

EVALUATION OF 3D TOOL WEAR IN MACHINING BY SUCCESSIVE STEREO-PHOTOGRAMMETRY AND POINT CLOUD PROCESSING

Damir Vučina, Dražen Bajić, Sonja Jozić, Igor Pehnc

Original scientific paper

The tool wear evaluation has a very strong impact on the product quality as well as efficiency of the manufacturing process. Experience-based assessment of tool wear and total cumulative time of operation has been applied. Tactile mechanical sensing devices and optical microscopes have been applied as well. This paper proposes and applies an innovative optical tool wear measurement method. It is based on 3D optical sensing using stereo-photogrammetry and triangulation. It offers high accuracy 3D dimensional deviation measurement spanning over the total tool surface, hence 3D deviation vectors from some reference shape are obtained simultaneously for millions of points. The overall tool wear shape function in 3D is generated, in many cases even without disassembly of the tool. Capturing the tool wear as a 3D shape function potentially offers abundant information towards diagnostics in terms of correlating the particular tool wear shape function with respective potential causes.

Keywords: 3D tool wear, end milling, stereophotogrammetry, surface deviation, wear diagnostic

Procjena trodimenzijskog trošenja alata u obradi odvajanjem čestica uporabom stereo-fotogrametrije i obrade oblaka točaka

Izvorni znanstveni članak

Procjena trošenja alata ima značajan utjecaj na kvalitetu proizvoda, kao i na učinkovitost proizvodnog procesa. Primijenjena je procjena trošenja alata temeljena na iskustvu i ukupnom vremenu trajanja obrade. Taktilni mehanički uređaji i optički mikroskop su također primijenjeni. Predlaže se i primjenjuje inovativna optička metoda mjerenja trošenja alata koja se zasniva na 3D skeniranju uporabom stereo-fotogrametrije i triangulacije. Metodom je moguće točno izmjeriti trodimenzionalne devijacije na ukupnoj površini rezne pločice, jer je trodimenzionalni vektor odstupanja oblika dobiven pomoću milijun točaka. Trodimenzionalnu funkciju sveukupnog istrošenja alata moguće je dobiti i bez uklanjanja alata s alatnog stroja. Određivanje istrošenja alata kao trodimenzionalne funkcije nudi mnoštvo informacija prema kojima je moguće dovesti u vezu pojedinačne oblike trošenja alata s mogućim uzorcima trošenja.

Ključne riječi: 3D trošenje alata, obodno glodanje, stereofotogrametrija, površinska odstupanja, dijagnosticiranje trošenja

1 Introduction

The final shapes of most machine elements are obtained by machining operations. In general, these operations involve one or more cutting edges in sliding contact with a workpiece material which is caused to shear by the cutting action. The selection of the applicable machining method depends on the required geometry, dimensional accuracy and surface quality of the part. These requirements are hard to achieve or even not feasible using other technologies like casting, sintering or metal forming.

Thanks to the development of the computer numerical control (CNC) machine tools, technology of computer aided design and computer aided manufacturing (CAD/CAM), as well as modern tools and technology of high speed machining, milling becomes indispensable and the most propulsive machining operation. Milling is generally used to produce parts which are not axially symmetric and have many features such as holes, slots, pockets and three dimensional surfaces contours. This process is capable of producing machine elements with complex shapes and high surface quality, such as molds and dies, gears, shafts, blades, etc.

The productivity of machining processes, as well as the integrity of the machined surface are strongly related to the tool wear and tool life. Tool wear hence becomes the key factor in the machining processes. If a worn tool is not identified beforehand, significant degradation of the workpiece quality can occur. Therefore, research in this area is still of great significance.

2 Tool wear

The cutting tool in any machining process is subjected to changes of its geometry and changes of respective material properties. Tribological processes leading to tool wear occur at rake and flank face, as it is shown in Fig. 1. Flank wear is caused by friction between the flank face of the tool and the machined workpiece surface and leads to the loss of the cutting edge. Therefore, flank wear affects the dimensional accuracy and surface finish quality. In practice, flank wear is generally used as the tool wear criterion. When the critical value of the tool wear criterion has been reached, the tool fails due to excessive stresses and thermal alterations caused by large friction forces. To avoid this, the cutting tool must be replaced before reaching its critical limit. However, this approach has two typical shortcomings. The first one is that a worn tool will produce out-of-specification parts or even cause catastrophic tool breakage. The second one is the fact that if the tool is dismissed prematurely, the direct consequence will be a significant waste of manufacturing resources [1].

In conventional machining, the process of tool wear consists of three stages, Fig. 2. These are the rapid initial wear, gradual intermediate wear and finally very rapid wear or catastrophic wear. The machining process needs to be stopped at the right time because of the consequences of the tool wear such as: increase of cutting forces, vibrations, noises, temperature in the cutting zone and deviation of part dimensions and surface quality from the respective tolerance values. As a results of the tool wear and combination of high temperatures and compression stresses, changes of the tool geometry

that cause plastic deformation in cutting are likely to occur.

There are several wear mechanisms that may occur simultaneously, whereby one of them may dominate the process. They can be listed as: mechanical wear (abrasion and adhesion), thermal-mechanical wear (fatigue), thermal-chemical wear (diffusion), electro-chemical wear (oxidation). Fig. 3 presents the dependence of the

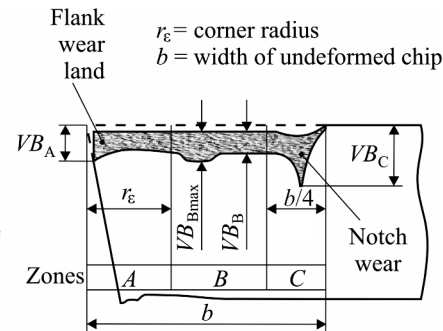
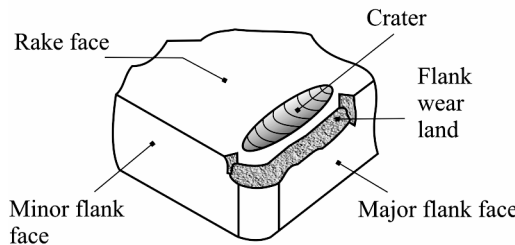


Figure 1 Form of tool wear [2]

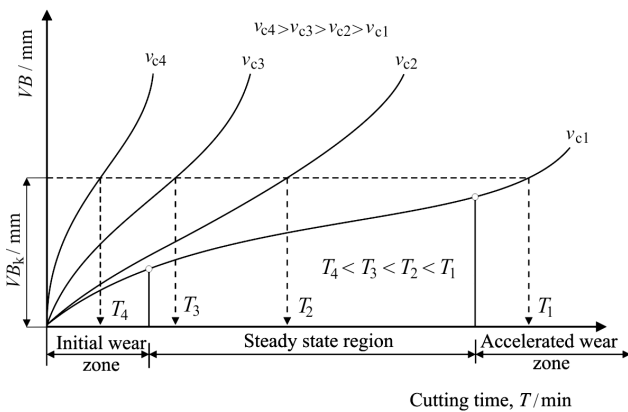


Figure 2 Tool life curves [1]

system consisting of a fiber-optic light source to illuminate the tool and a CCD camera which is used in combination with a high resolution of video zoom microscope. Identification of the tool wear area is based on the reflection from the wear area of the light introduced via fiber optics, whereas the measurements are derived from this area. Jurkovic et al. [9] presented a method of tool wear measuring using CCD vision system. The main parts of this systems are a light source used to illuminate the tool, CCD camera and laser diod with linear projector, grabber for capturing the picture, and a computer. They have developed a technique that can determine the profile deepness with the help of projected laser raster lines on a tool surface.

The proposed novel method which is described hereafter in detail belongs to direct methods. The added value and advantage of this method are the evaluation of 3D tool wear, as well as the subsequent computation of the weight loss of the tool inserts.

2.1 Tool wear in the milling process

The milling process is the most complex operation due to its intermittent nature, so additional factors affect the tool wear in this operation. In milling, the tool tooth periodically enters and exits the workpiece. Hence, it experiences stress and temperature cycling during cutting. This periodic coupled mechanical-thermal cycle produces alternating compression and tensile stresses on the tool that may exceed its strength. Even if the thermal stress amplitudes are not large enough to break the tool instantly, the thermal stress cycling causes gradual fatigue failure and wear of the tool. The temperature is a direct function of the relative speed and friction force between the materials in contact. Higher speeds result in more friction energy, which then increases the temperature at the contact zone between the workpiece and the tool. As the flank wear increases, the tool-workpiece contact area increases as well [1].

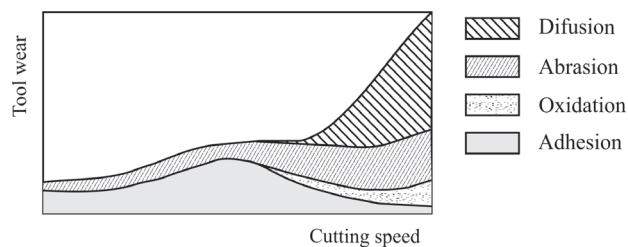


Figure 3 Tool wear mechanisms in dependence of cutting speed [3]

Tool wear can be measured using direct measuring techniques or estimated by indirect measuring techniques. In indirect measuring techniques, the tool wear is estimated using other easily measurable cutting process variables which are related to tool wear, such as the cutting force, acoustic emission, tool vibrations, etc. A survey of the literature indicates that many different approaches have been applied to tool wear prediction [4-7]. Direct measuring techniques, as the name implies, make an assesment of tool wear by either evaluating the worn surface by optical methods, or measuring the material loss of the tool by radiometric techniques. Direct methods require cutting operations to be interrupted periodically. Optical methods use optical equipment like the toolmaker's microscope, optical microscope, scanning electrical microscope, charged coupled devices (CCD cameras), etc. Kurada et al. [8] have designed a

3 Modelling of tool wear in machining

Many mathematical models have been developed to describe tool wear in quantitative terms. A lot of studies have been published by researchers who have attempted to directly correlate the amount of tool wear and tool life to the applied machining parameters, machining time, workpiece and tool materials, etc.

In order to measure the tool wear, a thorough understanding of the tool wear mechanisms at the tool edge is necessary.

Kwon and Fisher [10] have developed the tool wear index (TWI) and the tool life model, analyzing the wear surface areas and the tool material loss using micro-optics, image processing and an analysis algorithm. With relation to surface roughness, the TWI measures the minimum risk for in-process tool failure, and it is integrated in an optimal control strategy according to criteria of productivity improvement and reduction of manufacturing cost. Özel et al. [11] have investigated the influence of cutting parameters on the tool flank wear and surface roughness in finish turning of hard steel. Crater and flank wear of ceramic tool have been observed with scanning electron microscopy (SEM) after corresponding runs. Multiple linear regression models and neural network models have been developed for the prediction of tool flank wear and surface roughness. Similar modelling methodology and measuring techniques have been performed by Lajis et al. [12] in end milling of hardened steel. Nouari and Molinari [13] have investigated uncoated tool wear during machining of low-alloyed steel (DIN 42 CrMo 4, AISI 4140). The main influencing parameter on the diffusion wear has been the contact temperature. The temperature field has been simulated by means of the finite element method. As main parameters, the authors have used the contact length between the chip and rake interface, shear angle and width of removed material.

The tool wear rate has been modelled by Takeyama and Murata, [14]. They have set up the tool wear rate model considering the abrasive and the diffusive wear, as follows:

$$\frac{dW}{dt} = G(v_c, f_t) + D \cdot e^{-\frac{E}{R \cdot T}}, \quad (1)$$

with the following notation:

dW/dt – wear rate (volume loss of unit contact area per unit time)

$G(v_c, f_t)$ – function of cutting parameters,

D – workpiece material constant,

E – process activation energy, 75,35 kJ/mol,

R – universal gas constant, 8,314 kJ/(mol·K),

T – cutting temperature, K.

The well known Usui's tool wear rate model [14], presents the wear rate as a function of the output process variables such as T , σ_n , v_s ,

$$\frac{dW}{dt} = A \cdot \sigma_n \cdot v_s \cdot e^{-\frac{B}{T}}, \quad (2)$$

with:

A, B – empirical constants which depend on the combination of workpiece and cutting tool material,

σ_n – normal stress, MPa,

v_s – sliding speed, m/min.

In order to obtain the prediction model that relates the flank wear with the cutting parameters and machining time, design of experiments and regression analysis have been applied, [15]. After applying regression analysis on the experimentally determined data, the equation is defined as:

$$\begin{aligned} 1/B = & 0,02259 + 0,00038 \cdot v_c + 1,16017 \cdot f_t + 0,074675 \cdot a_e - \\ & - 0,00875 \cdot t - 0,0000023 \cdot v_c^2 - 12,31667 \cdot f_t^2 - 0,02079 \cdot a_e^2 + \\ & + 0,00012 \cdot t^2 + 0,0017 \cdot v_c \cdot f_t - 0,000215 \cdot v_c \cdot a_e - 0,000215 \cdot v_c \cdot a_e + \\ & + 0,000068 \cdot v_c \cdot t - 0,315 \cdot f_t \cdot a_e + 0,02625 \cdot f_t \cdot t + 0,00106 \cdot a_e \cdot t, \end{aligned} \quad (3)$$

with:

v_c – cutting speed, m/min,

f_t – feed per tooth, mm/tooth,

a_e – radial depth of cut, mm,

t – cutter engagement time, min.

4 3D digitizing, points cloud polygonization, repairs and processing of the mesh

Different 3D measurement techniques based on different physical principles have recently been introduced and successfully applied, [16–19]. The so-called ‘time-of-flight’ systems are built on temporal measurement for a laser beam, while triangulation-based systems use geometric entities such as distances and angles for measurement of position. These systems can be applied in rapid prototyping, digitizing of 3D shapes, inspection of shape deviation from reference samples, detection of geometric differences between physical objects and respective CAD models, monitoring of damage and wear via changes in shape, conversion of parts of objects into CAD models using best-fitting of parametric surfaces, creation of hybrid models by combining existing objects with numerically generated or re-engineered parts, shape optimization of parts of objects by engaging numerical optimizers acting on parametric surfaces, etc.

In this paper, it has been used the high resolution and high accuracy system ATOS [20], Fig. 4. The system implements a central projector and two cameras (with 1032×776 pixels resolution) and applies triangulation and stereo-photogrammetry for 3D reconstruction. The system is verified and calibrated according to the VDI 2634 standard. Different measurement volumes and corresponding sets of lenses can be used to provide a trade-off between efficient surface coverage using few successive scans and sufficient resolution and accuracy. The system utilizes projection of structured light patterns and time-based coding of positions of individual points, [17, 19], while reference points are applied to align and combine multiple scans into integral point clouds. The stripes projected onto the object are recorded as deformed (according to the shape of the object) by the cameras in the stereo-setup. The system is calibrated such that the

internal geometric parameters of the system such as camera angles and distances are determined in high precision based on 3D scan sequences of the corresponding calibration objects.

The time-based coding of spatial position of individual points can be implemented by projecting stripes whose light intensity varies with time such that the individual points receive a coding sequence in time, which represents their respective spatial position.



Figure 4 3D scanning using the ATOS system, reference points and structured light projection

The scan images originating at the two cameras can be used to generate-reconstruct the 3D model of the object surface. Geometric relationships between some 3D physical point and its 2D projections are defined by epipolar geometry. A mathematical model can be set up to map the 3D coordinates of a point into corresponding 2D projection points on the cameras, and reversely, given the two 2D projection points, the three coordinates of the corresponding spatial point can be reconstructed, Fig. 5.

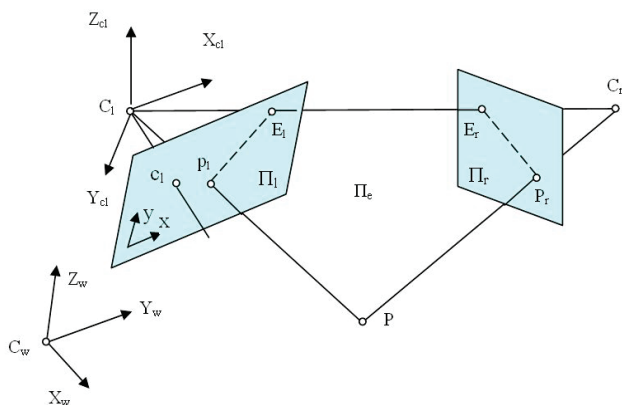


Figure 5 Basic entities with two-camera setup, 2D images of a 3D point, epipolar relationships

In Fig. 5, Π_l and Π_r are the image projection planes of the cameras, Π_e is the epipolar plane, C_l and C_r are the focal points of the cameras, w and c denote the world and camera coordinate systems respectively, the projection of C on Π is the principal point c . A general point $P(X,Y,Z)$ projects in the image plane into the point $p(x,y)$.

The following basic relationships can be established based on proportional triangles for a camera with focal length f ,

$$x = \frac{f \cdot X}{Z}, y = \frac{f \cdot Y}{Z}, z = f. \tag{4}$$

For a general point P given in the world coordinate system the coordinates in the (left) camera coordinate system are given by applying the corresponding translation matrix $T = C_w - C_l$ and the rotation matrix R ,

$$P_c = R \cdot (P_w - T), \tag{5}$$

with extrinsic camera parameters used in T and R . The mapping of the camera coordinates into the image plane coordinates (x_u, y_u) is based on intrinsic parameters including the focal length f and pixels dimensions (h_x, h_y)

$$x = (x_u - o_x) \cdot h_x, y = (y_u - o_y) \cdot h_y. \tag{6}$$

The final basic camera image equation is obtained as

$$p = M \cdot P, \tag{7}$$

with M as the projection matrix. Application of stereo-setup camera systems results in two sets of such equations that allow for the reverse operation, namely 3D reconstruction from 2D images. The position of the point P can be restricted to the line $C_l p_l$ and the line $C_r p_r$ and 3D reconstruction can be based on intersecting these two lines. The plane $C_l P C_r$ is called the epipolar plane and its intersections with the image planes Π the respective epipolar lines. The epipolar constraint restricts the image points p_i of a space point P somewhere on the epipolar lines of the image planes. For a left image point p_l , the matching image on the right camera must therefore be on the right epipolar line $\Pi_r \cap \Pi_e$.

3D reconstruction which recovers 3D Euclidean coordinates from stereo measurements can be done if all extrinsic and intrinsic parameters are calibrated. The principle of triangulation can provide the physical coordinates of the actual 3D point, which is located at the intersection of the rays through the image points from the camera centers,

$$P = L(p_l, p_r, c), \tag{8}$$

where L is the linear operator matrix for 3D reconstruction and c the calibration parameters.

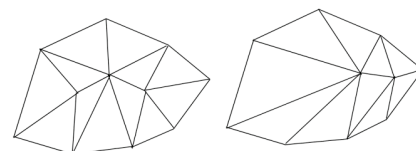


Figure 6 Polygonization and thinning of the mesh with smaller-size faces in areas with intensive change in slope and curvature

All surfaces of the object cannot be fully captured by a single 3D scan as some of them may not be visible. Therefore multiple 3D scans of the object from different positions are recorded and combined using at least three common reference points visible in successive scans, which are subsequently combined in the integral points

cloud. Polygonization reduces the overall point clouds to non-overlapping meshes of nodes and polygonal planar surface patches with C^0 continuity. The thinning of the points cloud and fitting of the mesh are based on least-

square optimization. Typically, in edge regions with higher curvature a more dense patchwork of smaller size polygons is used, Fig. 6.

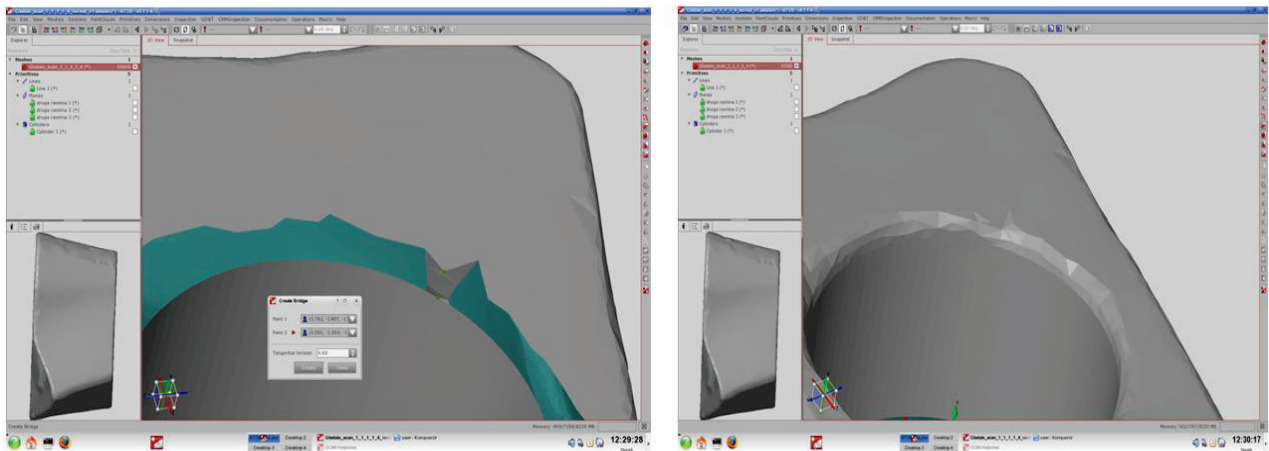


Figure 7 Creating bridges and interpolating faces to fill the voids in the point cloud after scanning

In many cases, there are small regions of the object which cannot be scanned successfully, and which are manifested as voids in the overall points cloud. These voids can be reconstructed numerically by generating mesh faces in those areas such that surface continuity and slope continuity with adjacent scanned areas is preserved. Filling of larger holes may require that bridges be created between opposite sides of the voids to reduce their size, Fig. 7.

Different meshes originating from 3D scanning and CAD primitives can be combined, provided that corresponding coordinate system transformations are carried out. The registration procedure combines multiple meshes for the purposes of combining them or to evaluate respective differences and deviations. Best-fit registration determines the relative degrees of freedom between the two coordinate systems such that the overall deviation between the selected parts of the two meshes is minimized.

Many authors, for example [21÷28], have proposed different algorithms and procedures for reverse engineering operations based on point clouds and polygonization meshes originating from 3D scanning, in most cases combined with geometric modelling, best-fitting and parameterizations.

5 Experimental setup

For the present work, all experiments were performed at the Tool machines laboratory and the Laboratory for optimization and design, both at the Faculty of Electrical

Engineering, Mechanical Engineering and Naval Architecture, Split. The machining center VC560 Spinner, equipped with a 12000 rpm electrospindle and the SK 40 tool holder, was used for the milling experiments. The end milling experiments were performed by the end mill CoroMill 390, R390-020A20-11M with three TiN coated inserts, marks R390-11 T3 08M-PM, produced by Sandvik. Inserts are with highly resistant coating made of TiN, which was in a thickness of 6 μm in the physical vapour deposition (PVD) process applied to the hard metal. Test samples made of steel 42CrMo4, with dimensions 250 \times 110 \times 110 mm, were prepared in order to remove rust, grooves and all damages from the surfaces which were to be machined. In each experiment, all of the tool inserts were new. The axial depth of cut was kept constant, $a_p = 5$ mm. The experiments were carried out without cooling and lubrication agent. The cutting conditions and experimental specifications are listed in Tab. 1. The cutting conditions have been selected according to the tool producer recommendations and considering the workpiece hardness. Hardness of the workpiece was 36 HRC. Machining tests were carried out to determine the flank wear under different cutting conditions and in different periods of cutter engagement.

The selected cutting parameters, shown in Tab. 1, correspond to the input variables that were used to obtain the regression equation (3). The milling process was discontinued periodically to remove the insert from the end mill for the purpose of tool wear measurement and scanning of the flank face.

Table 1 Experimental specifications and cutting conditions

v_c / m/min	f_t / mm/tooth	a_e / mm	t / min				Type of end milling	
100	0,02	1	5	10	20	25	30	Up milling
157	0,04	1	5	10	20	25	30	Up milling

6 Measuring of tool wear

6.1 Measuring of tool wear by means of USB camera

Using a USB camera is a feasible option to capture the image of the cutter and subsequently to analyse the

captured image. The applied USB system, Dino Lite, consists of a USB camera and corresponding software. The USB camera uses 200 \times magnification. The disadvantages of this method are the possibility of examining only one dimension at a time and a relatively

poor precision of wear evaluation. A cutter with a few measurements of flank wear is presented in Fig. 8. The obtained value depends on how precisely the zone of flank wear has been selected.



Figure 8 Flank wear obtained using the USB camera

6.2 Measuring of tool wear by means of portable measuring microscope

If a conventional microscope is used, it is possible to measure only the respective length and width of flank wear lands. Also, with conventional microscope measurement, the evaluation of accurate tool wear is time consuming, and depends on the respective researcher's experience or tiredness. The applied portable measuring microscope has a magnification of 100× and a measurement scale one millimeter in length with a minimum discernible division of 0,01 mm, Fig. 9. This method provides considerably more precise measurements, but the drawback is the possibility to evaluate only one dimension of flank wear at a time. Difficulties in measurement of flank wear also arise because of the irregular cutter shape due to the inadequate depth of the field microscope.



Figure 9 Portable measuring microscope

6.3 Measuring of tool wear based on stereo-photogrammetry and triangulation

The method elaborated in fourth Section is now applied to the scanning of the inserts. In order to evaluate wear, the 3D scans of two inserts were carried out successively after different periods of operation of the tool, according to Tab. 1. For each 3D scan, the tool was fixed in an adaptive fixation frame where the reference points have already been applied, Fig. 10. The object was covered with an extremely thin layer of titanium oxide

which had no impact on the results of this study, as it was applied both on the original and worn objects.

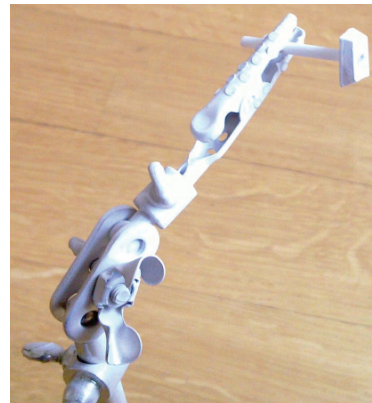


Figure 10 Adaptive frame with reference points fixing the milling tool for scanning

After successful calibration with deviation limits of 0,01 to 0,04 pixels, the measurement volume of the 65 × 50 × 30 mm was used with corresponding measurement object distance of 350 mm. Successive scans encapsulated at least three common reference points. The distance between cameras for a given measurement volume is based on SO mount available. While a smaller measurement volume would have provided a denser point cloud, the one obtained here proved to be quite adequate. Fig. 11 shows a resulting points cloud after 3D scanning. Fig. 11a shows the integral points cloud, and Fig. 11b points out the portions of the 3D cloud that were dismissed from further processing as they belong to the fixation frame rather than the tool itself.

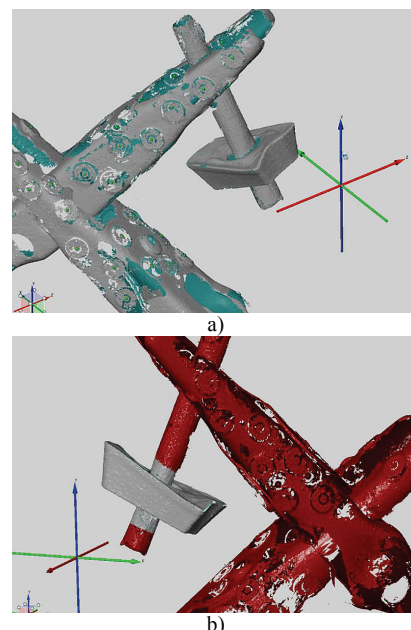


Figure 11 Points cloud after 3D scanning, a) full cloud, b) selected portion for further analysis

Fig. 12a shows the 3D points cloud of the tool itself after all the points which do not belong to the tool have been removed, while Fig. 12b shows the corresponding mesh after filling the voids and polygonization.

After the individual scans have been processed, as shown in Figs. 11 ÷ 12, the surface deviations with respect to the reference shape for the two selected tool inserts can be evaluated. In order to do this, those different 3D scans need to be imported into a common reference coordinate system and mutually aligned.

First, the holes in the tool inserts that serve the purpose of fixation onto the end mill and which were not accessible (visible) for scanning, Figs. 11 ÷ 12, were closed by best-fitting cylinders available as CAD primitives.

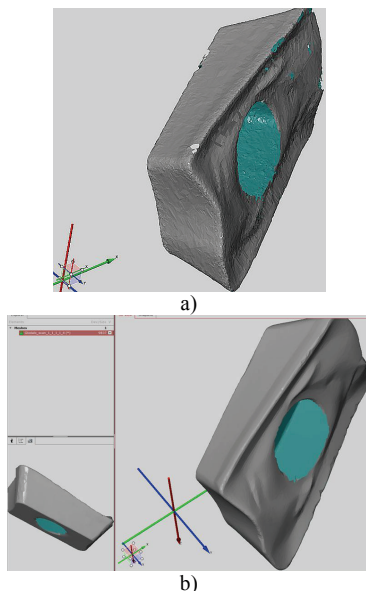


Figure 12 a) Points cloud of the insert, b) Corresponding mesh after polygonization

Those cylinders were subsequently tessellated and the resulting meshes were combined with the scalling meshes. The overall mesh now represents closed objects the respective volumes of which can be calculated. However, it was established that the volume loss of the inserts due to wear that could be calculated using this procedure was not relevant for estimation of wear intensity. The cause for this is the fact that the volume loss values were to small and insignificant when compared to numerical errors due to closing the holes in the mesh, mesh patches interpolations and similar approximate geometric operations. Therefore, 3D dimensional deviations with respect to the reference shape which were captured from the 3D scans were considered more reliable and relevant for tool wear assessments.

Now, the definition of the common coordinate system can be established such that it applies to all scans in a unified manner. Best-fit plane segments with fixed dimensions were first generated at the lateral surfaces of the tool inserts, Fig. 13. Then, a line was generated through the central points of the best-fit plane segments.

A third best-fit plane segment with fixed dimensions was generated on the upper surface of the tool insert, Fig. 14. The central point of this plane segment was selected as the final entity for the definition of the common reference coordinate system based on the plane-line-point coordinate transformation. The described computational geometry entities (planes, lines, intersections), uniquely define the same coordinate system of all objects.

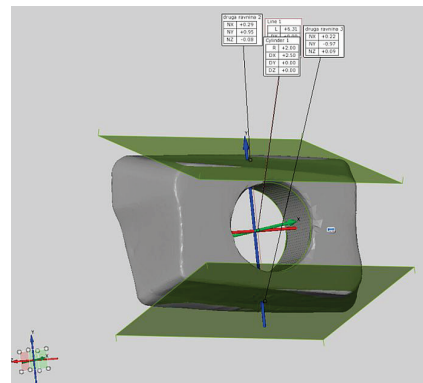


Figure 13 Best-fitting plane segments at curved lateral surfaces of the tool insert and generating the common y-axis

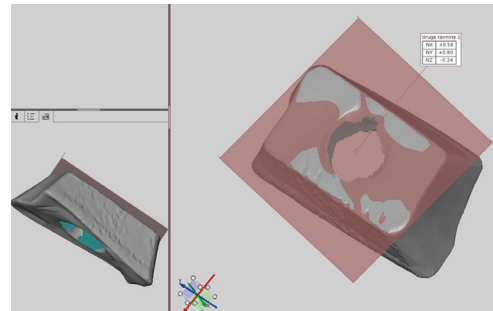


Figure 14 Best-fitting a plane segment at the top surface of the insert

The quality of the best-fit operation would deteriorate otherwise as the portions with significant wear would have an impact as the algorithm would try to best-fit them as well.

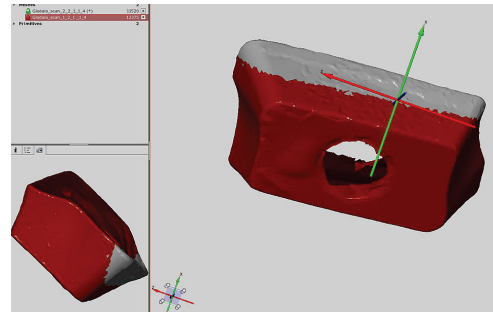


Figure 15 Parts of the overall meshes participating in best-fitting different meshes of the tool inserts

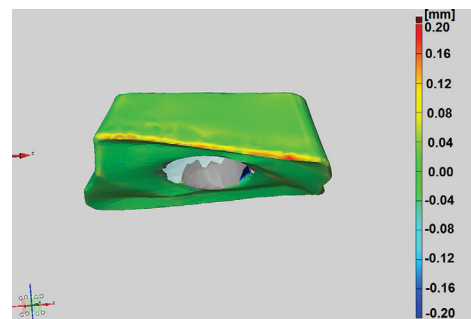


Figure 16 Surface deviation plot, initial shape vs. shape after 20 minutes of milling operation in regime

Now, with all of the scans in the same common reference coordinate system the evaluations of the surface deviations can be carried out. In order to do this, the meshes that belong to different scans need to be mutually aligned in high precision and accuracy. When aligning two meshes that belong to the same tool insert but differ

chronologically in terms of duration of milling operation performed and hence wear, only the parts of the total respective shapes without significant wear were included for the best-fit registration of the two meshes, Fig. 15.

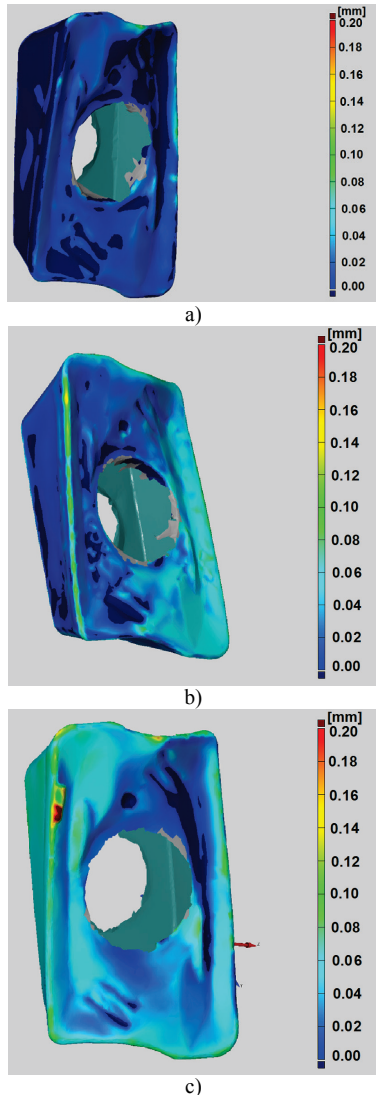


Figure 17 Surface deviation plots showing incremental magnitude of tool wear, a) after 10 minutes, b) after 20 minutes, c) after 25 minutes of cutter engagement time

Now the actual surface deviation operation can take place. Fig. 16 shows the typical surface deviation plot

whereby the cutting edge of the tool shows the largest deviations with respect to its initial shape. Fig. 16 shows the deviations as absolute displacements between matching points which can also be decomposed into individual coordinate directions.

The following figures present some of the results of 3D surface deviation plots that are here used to quantify the respective tool wear. The developed procedure shows obvious advantages over classical methods as higher accuracy is possible, 3D deviations are provided instead of 1D, and deviations of millions of points are obtained simultaneously (depending on measurement resolution). Moreover, parameterization of the surface deviation and parametric offset surfaces can be conclusive in terms of possible causes of irregular tool wear. Fig. 17a shows the surface deviation of the tool insert after 10 minutes of operation as compared to the shape after 5 minutes of operation. This plot can be used to estimate the incremental wear of the tool, both in terms of its quantification and localization. Fig. 17b presents the incremental magnitudes of tool wear after 20 minutes of operation as compared to the shape after 5 minutes of operation, Fig. 17c presents the incremental magnitudes after 25 minutes of operation.

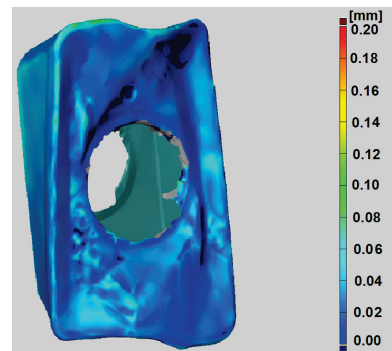


Figure 18 Comparison of tool wear of two different inserts engaged in the same milling operation simultaneously

Finally, Fig. 18 presents the tool insert wear of two different inserts engaged in the same milling operation simultaneously, proving the tool insert wear to be rather uniform for different (here adjacently located) tools.

Table 2 Results of flank wear measurements for the first insert

Cutting conditions					Flank wear, VB / mm			
Exp. No.	v_c / m/min	f_t / mm/tooth	a_e / mm	t / min	USB camera	Microscope	3D edge area	Model eq. (3)
1	100	0,02	1	10	0,08	0,09	0,08 ÷ 0,12	0,09
				20	0,12	0,12	0,10 ÷ 0,14	0,12
				25	0,13	0,16	0,16 ÷ 0,20	0,15
2	157	0,04	1	10	0,10	0,12	0,08 ÷ 0,14	0,12
				20	0,18	0,20	0,14 ÷ 0,18	0,19
				25	0,23	0,25	0,18 ÷ 0,24	0,24

7 Evaluation of results and discussion

Experiments and measurements were carried out according to Tab. 1. Summary of the measured values and values obtained by means of model (3) is given in Tab. 2. It is obvious that the methods provide mutually similar

wear magnitudes in terms of linear deviations at selected locations. However, 3D scanning provides point wear magnitudes as spatial displacement vectors and does this simultaneously for a huge points cloud of the tool at the given high accuracy and resolution. The spatial wear vectors obtained this way can therefore be interpreted as

wear functions defined on the given spatial domain, and this approach consequently delivers much more information than the classical wear measurement methods. Based on algorithms that automatically evaluate the rich 3D point clouds for a particular milling condition, such abundance of wear-related information could potentially be processed by a programmed analysis procedure and lead to conclusions related to respective causes and modes of wear.

8 Conclusions

The proposed 3D tool wear measurement using stereo-photogrammetry and triangulation, capturing the entire tool surface in a single run, offers high resolution and accuracy 3D dimensional deviation measurement spanning the overall tool surface. It outperforms traditional 1D deviation methods both in accuracy and especially in efficiency. Another huge benefit of the developed method is the fact that each individual scan can be done in less than a second without even disassembling the tool from the machine. The sequence of individual scans can generally be performed automatically using rotating table positioning mechanism and a program script.

Future work will be focused on developing computational procedures for the analysis of spatial deviation data provided by the optically acquired 3D tool wear shape function. The objective is automatic diagnostics and early alert pointing to possible tool damage, excessive local tool wear, tool misalignment and other possible causes for the acquired mode of the tool wear shape function based on corresponding correlation.

Acknowledgments

This work was supported in part by the Croatian Ministry of Science, Education and Sports, project number 023-0231744-3113, Intelligent and Evolutionary Algorithms in Optimization and project number 023-0692976-1742, Investigation of highspeed machining.

The authors also wish to thank mr. Mario Milinović, graduate student, for his assistance with the test examples.

9 References

- [1] Altintas, Y. *Manufacturing Automation*, University of British Columbia, University Press, Cambridge, 2000.
- [2] Grote, K. H.; Atonsons, E. K. *Handbook of mechanical engineering*, Springer, New York, 2009.
- [3] Ekinović, S. *Obrada rezanjem, Dom štampe Zenica*, Zenica, 2001.
- [4] Li, X.; Ouyang, G.; Liang, Z. Complexity measure of motor current signals for tool flute breakage detection in end milling. // *International Journal of Machine Tools and Manufacturing*, 48, (2008), pp. 371-379.
- [5] Mathew, M. T.; Srinivasa Pai, P.; Rocha, L. A. An effective sensor for tool wear monitoring in face milling: Acoustic emission. // *Sadhane*, 33, (2008), pp. 227-233.
- [6] Lin, S. C.; Lin, R. J. Tool wear monitoring in face milling using force signals. // *Wear*, 198, (1996), pp. 136-142.
- [7] Dimla Sr., D. E.; Lister, P. M. On-line metal cutting tool condition monitoring (I): force and vibration analysis. // *International Journal of Machine tools and Manufacturing*, 40, (2000), pp. 739-768.
- [8] Kurada, S.; Bradley, C. A machine vision system for tool wear assessment. // *Tribology International*, 30, (1997), pp. 295-304.
- [9] Jurkovic, J.; Korosec, M.; Kopac, J. New approach in tool wear measuring technique using CCD vision system. // *International Journal of Machine Tools & Manufacture*, 45, (2005), pp. 1023-103.
- [10] Kwon, Y.; Fischer, G. W. A novel approach to quantifying tool wear and tool life measurements for optimal tool management. // *International Journal of Machine Tools & Manufacture*, 43, (2003), pp. 359-368.
- [11] Özel, T.; Karpat, Y.; Figueira, L.; Davim, J. P. Modelling of surface finish and tool flank wear in turning Tool life and tool wear in the semi-finish milling of inclined surfaces. // *Journal of Materials Processing Technology*, 209, (2009), pp. 5448-5455.
- [12] Lajis, M. A.; Mustafizul Karim, A. N.; Nurul Amin, A. K. M.; Hafiz, A. M. K.; Turnad, L. G. Prediction of Tool Life in End Milling of Hardened Steel AISI D2. // *European Journal of Scientific Research*, 21, (2008), pp. 592-602.
- [13] Nouari, M.; Molinari, A. Experimental verification of a diffusion tool wear model using a 42CrMo4 steel with an uncoated cemented tungsten carbide at various cutting speeds. // *Wear*, 259, (2005), pp. 1151-1159.
- [14] Takeyama, H.; Murata, T. Basic investigations on tool wear. // *Transaction of ASME J. Eng. Ind.* 85, (1963), pp. 33-38.
- [15] Topić, S. *Modeling of tool wear in milling process*. Thesis, Faculty of Electrical Engineering, Mechanical Engineering and Naval Architecture, Split, 2011.
- [16] Cyganek, B.; Siebert, J. P. *An introduction to 3D computer vision techniques and algorithms*, John Wiley & Sons, Ltd, 2009.
- [17] Peng, T.; Gupta, S. K. Model and algorithms for point cloud construction using digital projection patterns. // *ASME Journal of Computing and Information Science in Engineering*, 7, (2007), pp. 372-381.
- [18] Zhang, Z. Determining the Epipolar Geometry and its Uncertainty: A Review. // *International Journal of Computer Vision*, 27, (1998), pp. 161-198.
- [19] DePiero, F. W.; Trivedi, M. M. 3D Computer Vision Using Structured Light: Design, Calibration and Implementation Issues. // *Advances in Computers*, 43, (1996), pp. 243-278.
- [20] GOM, GOM Atos manuals, www.gom.com, 2011.
- [21] Rogers, D. F. *An Introduction to NURBS With Historical Perspective*, Academic Press, San Diego, 2001.
- [22] Sarkar, B.; Menq, C-H. Smooth-surface approximation and reverse engineering. // *Computer-Aided Design*, 23, (1991), pp. 623-628.
- [23] Eck, M.; Hoppe, H. Automatic Reconstruction of B-Spline Surfaces of Arbitrary Topological Type, ACM SIGGRAPH 1996 Conference Proceedings, pp. 325-334. <http://research.microsoft.com/en-us/um/people/hoppe/proj/bspline/>, 2011
- [24] Kruth, J. P.; Kerstens, A. Reverse engineering modelling of free-form surfaces from point clouds subject to boundary conditions. // *Journal of Materials Processing Technology*, 76 (1998), pp. 120-127.
- [25] Dan, J.; Lancheng, W. An algorithm of NURBS surface fitting for reverse engineering. // *Int J Adv Manuf Technol*, 31, (2006), pp. 92-97. DOI 10.1007/s00170-005-0161-3
- [26] Varady, T.; Martin, R. R.; Cox, J. Reverse engineering of geometric models - an introduction. // *Computer-Aided Design*, 29, (1997), pp. 255-268.
- [27] Ma, W.; Kruth, J. P. NURBS curve and surface fitting for reverse engineering. // *International Advanced Manufacturing Technology*, 14, 12(1998), pp. 918-927.
- [28] Ristic, M.; Brujic, D. Efficient registration of NURBS geometry. // *Image vision comput*, 15, (1997), pp. 925-935.

Authors' addresses***Damir Vučina, PhD, Full Professor***

Faculty of Electrical Engineering, Mechanical Engineering and
Naval Architecture
Department of Mechanical Engineering and Naval Architecture
Rudera Boškovića 32
21000 Split, Croatia
tel. +385 21 305 969
fax. +385 21 305 776
E-mail: vucina@fesb.hr

Dražen Bajić, PhD, Full Professor

Faculty of Electrical Engineering, Mechanical Engineering and
Naval Architecture
Department of Mechanical Technology
Rudera Boškovića 32
21000 Split, Croatia

Sonja Jozić, PhD, Assistant Professor

Faculty of Electrical Engineering, Mechanical Engineering and
Naval Architecture
Department of Mechanical Engineering Technology
Rudera Boškovića 32
21000 Split, Croatia

Igor Pehcec, PhD, Assistant

Faculty of Electrical Engineering, Mechanical Engineering and
Naval Architecture
Department of Mechanical Engineering and Naval Architecture
Rudera Boškovića 32
21000 Split, Croatia